Design and Fabrication of Biomimicking Radially Graded Scaffolds via Digital Light Processing for Bone Regeneration

Yue Wang [1, 2], Shangsi Chen[2], Haowen Liang[1], Jiaming Bai [1, *], Min Wang [2, *]

[1] Department of Mechanical and Energy Engineering, Southern University of Science and Technology, Shenzhen, 518055, China

[2] Department of Mechanical Engineering, The University of Hong Kong, Pokfulam Road, Hong Kong

---

* Corresponding Author:

[1] Jiaming Bai, at the Southern University of Science and Technology Email: baijm@sustech.edu.cn Tel: 0755-88015354

[2] Min Wang, at the University of Hong Kong, Hong Kong Email: memwang@hku.hk Tel: 852-39177903

Abstract

Scaffolds are an essential component in bone tissue engineering (BTE). However, most of the current BTE scaffolds are homogeneous structures and do not resemble the graded architectures of native bone. In the current study, four types of biomimicking scaffold designs based on gyroid (G) and primitive (P) units with radially graded pore sizes were devised, and scaffolds of these designs with two porosity groups (65 vol.% and 75 vol.%) were fabricated via digital light processing (DLP) 3D printing using biphasic calcium phosphate (BCP). Scaffolds of the Gyroid-Gyroid (G-G) design displayed better dimensional accuracy, compressive property, and cell proliferation rate than Gyroid-Primitive (G-P), Primitive-Gyroid (P-G), and Primitive-Primitive (P-P) scaffolds. Subsequently, graded G-G scaffolds with different porosities were fabricated and the relationship between compressive strength and porosity was determined. Furthermore, the sintered BCP bioceramics fabricated via current manufacturing process exhibited excellent biocompatibility and bioactivity, indicating their high potential for BTE.

Keywords: biomimicking scaffold, radial gradient, triply periodic minimal surface, biphasic calcium phosphate; digital light processing

1. Introduction

Bone defects and injuries are commonly encountered in the medical field, and large bone defects in humans cannot heal naturally. At present, the main methods for treating bone defects are the use of autografts, allografts and synthetic biomaterials, with bone tissue engineering (BTE) showing great potential [1, 2]. However, autografts are limited by their source, and allografts face immune-associated risks. Therefore, BTE has been considered as a good alternative for bone tissue repair through the synergistic use of cells, scaffolds, and biomolecules (e.g. growth factors)[3]. Scaffolds play an essential role in BTE since they can provide a conductive environment for seeded cells until the new bone restores the functions of bone at the defect site [4, 5]. Although many types of BTE scaffolds have been developed, most of them exhibit simple and homogeneous structures that do not resemble the graded architectures of native bones [6]. Human bone has a typical heterogeneous structure and exhibits a radial gradient of pores from the exterior cortical bone to the interior cancellous bone, accompanied by an increase in pore size and porosity [7]. As porosity, pore size and pore interconnectivity are critical for bone tissue neo-formation and thus significantly affect bone remodeling, it is necessary to design functionally graded scaffolds (FGS) to mimic the structures and functions of native bone and facilitate cells behaviors [8, 9]. However, the graded scaffold-related studies have been rarely

reported owing to the fabrication limitations of traditional scaffold fabrication techniques.

Additive manufacturing (AM), which has developed rapidly over the past two decades, provides a powerful platform for accurate fabrication of customized structures and geometries. Among various AM technologies, direct ink writing (DIW) and selective laser melting (SLM) have been widely reported for fabricating graded scaffolds. However, DIW can only be implemented to produce simple gradients by varying the spacing between adjacent struts or strut diameters, and it is hard to use DIW to develop scaffolds with customized complex geometries, such as lattice or other bio-inspired graded structures [10, 11]. Currently, SLM has been extensively employed for the manufacture of metallic graded scaffolds with complex geometries and high mechanical properties. For example, Zhang *et al*. produced a parametric design of FGS and fabricated the scaffolds via SLM using Ti6Al4V powder [12]. Their scaffolds showed comparable mechanical properties and permeability with native bone tissue. Li *et al*. demonstrated that graded iron scaffolds could be fabricated via SLM [13]. The mass transport properties, biodegradation behaviors and mechanical properties of the scaffolds could be tuned through topological design with functional gradients. However, metal materials that commonly used for SLM, e.g., stainless steels, cobalt-chromium alloys, Ti and Ti alloys are bio-inert and have minimal

interactions with surrounding tissues in the body, resulting in poor osteo-conductivity, corrosion and even implant loosening over time [14]. Recently, ceramic fabrication via vat photopolymerization (VPP) 3D printing has progressed rapidly and provided a novel way for preparing graded ceramic parts. Wang *et al*. fabricated graded porous hardystonite implants based on I-graph and wrapped package-graph (IWP) unit cell for orbital reconstruction in the body and their study suggested hardystonite scaffolds with graded pore designs had the potentials as the next-generation orbital implants [15]. Among bioceramics, biphasic calcium phosphate (BCP) is a promising bioactive material for BTE scaffolds owing to its advantages as a hybrid of hydroxyapatite (HAp) and β-tricalcium phosphate (β-TCP), which includes good biocompatibility, osteoconductivity, and controllable biodegradation rate [16-18]. It has been considered as an excellent material for bone tissue repair [19, 20]. Digital light processing (DLP) is an effective VPP-based 3D printing technology to fabricate complex ceramic structures with high accuracy and fidelity [21, 22]. Therefore, the fabrication of graded BCP scaffold via DLP 3D printing should be systematically explored.

Advances introduced by computer-aided design (CAD) enable more design freedom and make it possible to tailor the scaffold structures with graded features. Currently, lattice structures, triply periodic minimal surfaces (TPMS), and voronoi-based structures are investigated for graded tissue engineering scaffolds [23-25]. Among

these new designs, TPMS has attracted more attention owing to its large surface area which is beneficial for cell adhesion and spreading in pores. The intrinsic complexities and high specific tortuosities can obviously increase the permeability and enhance nutrient and oxygen diffusion [26]. Besides, the TPMS structure may offer a better mechanical performance through structural optimization. Zhang *et al.* demonstrated that TPMS-based HAp scaffolds exhibited a greater compressive strength range than traditional cross-hatch structures [27]. Gyroid (G) and primitive (P) are two popular TPMS-based structures for graded scaffold designs. Vijayavenkataraman *et al*. designed a P-based graded structure for hip implants to mitigate stress-shielding effects. However, they only proposed the 3D models without actually fabricating the scaffolds [28]. Liu *et al.* explored a pore size longitudinal gradient based on G structure for bone graft and fabricated the scaffolds via SLM using Ti6Al4V powders [24]. They demonstrated that TPMS was a feasible way to realize gradients in multiple patterns and was potentially useful for mimicking properties of the host bone. However, the idea of combining the advantages of TPMS structure and bioactive ceramics for biomimicking radially structural gradient of native bone has so far not been explored.

In the current study, based on TPMS-G and -P units, four biomimicking scaffold designs with radial gradients to mimic the graded features of native bone for BTE

were made. The pore size and porosity could be simultaneously controlled in a specific range. Scaffolds based on these designs with two porosity groups (65 vol.% and 75 vol.%) were fabricated via DLP 3D printing. The formulated BCP slurry had a low viscosity and good curing accuracy, which enabled the successful fabrication of the graded scaffolds with high fidelity. Graded G-G scaffolds showed a better dimensional accuracy, compressive property, and cell proliferation rate than graded G-P, P-G and P-P scaffolds because of the inherent geometrical features. The sintered BCP bioceramics via current manufacturing process exhibited excellent biocompatibility and bioactivity.

2. Materials and Methods

2.1 Materials

The nano-sized HAp powders are 20 nm in diameter and 270 nm in length, and the average particle size of β-TCP powders is 500 nm. They were purchased from Nanjing Emperor Material Company. The organic reagents for photosensitive slurry preparation, isobornyl acrylate (IBOA), 1, 6-hexanediol diacrylate (HDDA), polyethylene glycol diacrylate (PEGDA), and 2,4,6-trimethyl-benzoyl-diphenylphosphine oxide (TPO) were provided by Shanghai Yinchang New Material Co., Ltd. A commercial dispersant BYK 111 (BYK Chemie, Germany) was applied for slurry dispersion. All chemicals were used as received without further processing.

2.2 CAD model design of radially graded scaffolds

The TPMS-G and TPMS-P surface were employed in the current study for graded scaffold design, which could be described by the following mathematic equation, respectively [26]:

$$\text{G: } \cos(\omega x)\sin(\omega y) + \cos(\omega y)\sin(\omega z) + \cos(\omega z)\sin(\omega x) = c \quad (1)$$

$$\text{P: } \cos(\omega x) + \cos(\omega y) + \cos(\omega z) = c \quad (2)$$

where, ω is related to the unit cell size, c defines the surface expansion in three dimensions [29]. Here, $c = 0$.

To realize the radial gradient between G and P structure, the entire structure is described by one continuous function $\emptyset_{graded}$:

$$\emptyset_{graded} = \partial_{(x,y,z)}\emptyset_{1(x,y,z)} + (1 - \partial_{(x,y,z)})\emptyset_{2(x,y,z)} \quad (3)$$

$$\partial_{(x,y,z)} = \frac{1}{1+e^{-k\cdot G(x,y,z)}} \quad (4)$$

where, $G(x, y, z) = 0$ controls the transition boundary between $\emptyset_{1(x,y,z)}$ and $\emptyset_{2(x,y,z)}$. The constant *k* describes the transition mutability. A small *k* results in a big transition zone and slow shape change, and vice versa [30]. To obtain a smooth transition, k was set to 0.1 in the current study. MATLAB software was used to create models for graded structures by adjusting different function parameters, and Magics software was applied to regulate and prepare stereolithography (.STL) files.

According to the graded features of human long bone [31], the BTE scaffolds with radial gradients from the center to the perimeter in this study were divided to three layers (figure 1): marrow cavity layer (layer 1), cancellous bone layer (layer 2) and cortical bone layer (layer 3). Four types of biomimicking radially graded scaffold designs based on G and P units were proposed in this study, namely G-G, G-P, P-G, and P-P according to the surface type of inner and outer region, as shown in figure 1. In the current study, 3D models with two porosity groups (65% and 75%) of those four types of graded scaffolds were designed. For each group, porosity and pore size were simultaneously controlled in a specific range via varying unit cell size and wall thickness. Graded G-G scaffolds with different porosities (50%, 55%, 65%, and 75%) were also designed via same procedures.

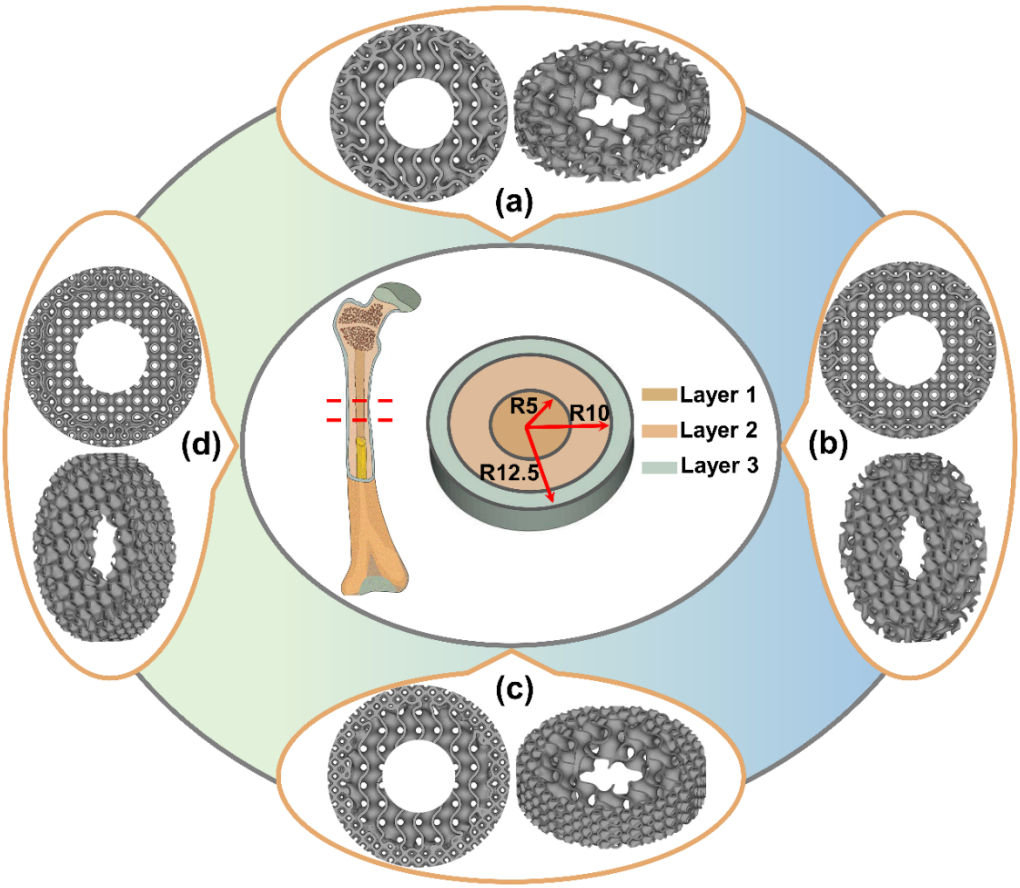

Figure 1. Top and side views of four types of radially graded scaffold 3D models according to three layers distribution using TPMS. (a) G-G. (b) G-P. (c) P-G. (d) P-P.

2.3 Slurry preparation and scaffold fabrication

Before slurry preparation, ceramic powers were dried in an oven at 80℃ for 24 h to remove the moisture. The BCP slurry was made by mixing IBOA, HDDA, PEGDA, TPO (photo-initiator), BYK 111 (dispersant), HAp, and β-TCP powders (HAp/β-TCP weight ratio of 50/50) via planetary ball milling machine (QM-3SP2, Nandu instrument plant, China) at a speed of 400 rpm/min for 12 h. The weight ratio

of hybrid resin matrix was IBOA: HDDA: PEGDA= 1:3:1.1 wt.% of TPO relative to the mass of the resin was added. 4 wt.% of BYK 111 based on the mass of the ceramic powders was utilized for slurry dispersion. Herein, BCP slurry with 70 wt.% solid loading was prepared according to the above procedure. The final formulation of 70 wt.% solid loading BCP slurry contained 35 wt.% HAp powders and 35 wt.% β-TCP powders (HAp: β-TCP=1:1), 2.8 wt.% BYK 111 (4 wt.% relative to weight of BCP powders), 0.27 wt.% TPO (1 wt.% relative to weight of resin), 5.39 wt.% IBOA, 16.15 wt.% HDDA, and 5.39 wt.% PEGDA (IBOA: HDDA: PEGDA=1:3:1).

3D CAD models were sliced and transferred to a home-made top-down DLP printer. When the printing started, the platform was positioned one layer lower than the slurry surface. Then, the UV light selectively exposed a defined pattern on the slurry surface and initiated the photopolymerization according to the 3D sliced data. After one layer of exposure, the platform was lowered by one layer thickness, and a scraper moved to recoat for printing the next layer. The printing continued layer-by-layer by repeating the process till completion. Finally, the green bodies were removed manually from the DLP machine and ultrasonically cleaned in a bath containing 50 vol % ethanol and 50 vol % HDDA.

Afterwards, the green bodies were transferred to a debinding furnace (L40/11 BO, Nabertherm, Germany) with heating from 50 ℃ to 700 ℃ and subsequently

sintered at 1200 ℃ for 2 h in a sintering furnace (LHT 04/17, Nabertherm, Germany). Figure 2 shows the schematic diagram of graded BCP scaffolds prepared by DLP 3D printing.

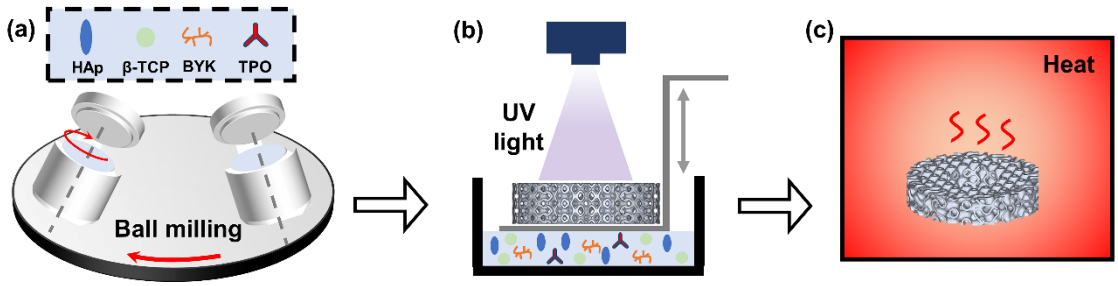

Figure 2. Schematic illustration of the fabrication of radially graded BCP scaffolds via DLP. (a) BCP slurry preparation. (b) DLP 3D printing. (c) Ceramic debinding and sintering.

2.4 Characterization

Viscosity of BCP slurry was studied through a rotational rheometer (MCR-92, Anton Paar GmbH, Austria). The shear rate range was 1 s^{-1} - 100 s^{-1}. A micrometer caliper (MDC-25PX, Mitutoyo, Japan) was used to measure the cure depth of one cured layer. The thermal decomposition behavior of the green body was explored using a thermogravimetric analyzer (Discovery TGA, TA Instruments, US) from 50-700℃ at a heating rate of 10 °C/min. To confirm the phases in the sintered BCP scaffolds, X-ray diffraction (XRD, SmartLab, Japan) analysis with scanning ranging from 20° to 60° was performed. The mass fraction of the main phases in the sintered

scaffolds was calculated using the adiabatic method [32]. If there are only two phases in the samples, the mass fraction of phase A and phase B can be calculated using following equations [20]:

$$W_A = \frac{I_A}{I_A + \frac{I_B}{K_A^B}} \quad (5)$$

$$W_B = 1 - W_A \quad (6)$$

$$K_A^B = \frac{RIR_B}{RIR_A} \quad (7)$$

where W_A and W_B are the mass fraction of phase A and phase B, respectively. I is the integrated intensity of the strongest peak of the phase. The reference intensity ratio (RIR) of HAp and β-TCP is 1.10 and 1.20, respectively.

The microstructure of the sintered scaffolds was observed via a scanning electron microscope (SEM, Apreo2 S Lovac, Thermo Fisher Scientific, US). The chemical composition was detected using energy dispersive X-ray spectroscopy (EDS). The pore size of scaffolds was measured via software Nanomeasure based on SEM images. At least four samples were analyzed for obtaining an average.

The designed porosity of the 3D models of the radial scaffolds was obtained using the Magics software. Their actual porosity was calculated via mass measurement using following equations [33]:

$$Real\ porosity = \left(1 - \frac{V_{scaffold}}{V_{total}}\right) \times 100\% \quad (8)$$

$$V_{scaffold} = m_{scaffold}/\rho \quad (9)$$

$$V_{total} = \pi(R^2 - r^2) \times H \quad (10)$$

where $m_{scaffold}, R, r, H \; and \; \rho$ are the weight, outer radius, inner radius, height of porous sintered scaffolds and density of BCP (3.15 g/cm^3), respectively. Four samples were analyzed for an average. For each sample, $R, r, and \; H$ were measured three times for an average. The compressive tests were performed through a universal testing machine (E45.504, MTS Systems, China) at a loading speed of 0.25 mm/min. Porous radial scaffolds with a diameter of 25 mm, a height of 4 mm, and a hollow central diameter of 10 mm was compressed. The compressive strength was obtained by the maximum stress value and Young's modulus was the slope of the linear part of the stress-strain curve. At least five samples for each type were tested. The volume density of the sintered bulk BCP ceramics (Φ 10 × 1.5 mm) was calculated according to Archimedes' method:

$$Volume \; density = \frac{M_d \times \rho_l}{M_d - M_l} \quad (11)$$

where, M_d represents the weight of samples in the dry state and M_l is the weight of the submerged samples. ρ_l is the liquid density that used for submerging. Here, ethanol was adopted in the current study.

2.5 Bioactivity evaluation

To investigate the potential bioactivity of the scaffolds prepared by current fabrication process, the BCP samples were immersed in the simulated body fluid

(SBF) solution at 37℃ water baths for 72 h. Subsequently, the samples were rinsed three times with deionized water and then dried overnight at 70 ℃. Finally, the bone-like apatite forming on the ceramic surface was observed by SEM and detected by EDS.

2.6 Cell culture

To study the biocompatibility and cytotoxicity of the BCP ceramics and scaffolds fabricated via current fabrication process, mouse pre-osteoblasts, MC3T3-E1 cells, were used in this study. The cells were cultured in Alpha Minimal Essential Medium (α-MEM, Gibco) supplemented with 10% fetal bovine serum (FBS, Gibco) and 1% penicillin/streptomycin (Invitrogen, USA) at 37 °C under a 5% CO_2 atmosphere.

To explore the cell proliferation behavior of the material, MC3T3-E1 cells were seeded onto the BCP ceramic bulk disks (Φ 6 × 1 mm) and blank culture plate (as control) at a density of 2×10^3 cells/well in the 96-well plate. After 1, 3, and 5 days of incubation, cell proliferation was evaluated by cell counting kit-8 (CCK-8). The absorbance was determined at 450 nm using a Cytation 1 Cell Imaging Multi-Mode Reader.

To evaluate the cell viability on BCP ceramics, MC3T3-E1 cells were seeded on bulk BCP samples (Φ 10 × 1 mm) in the 48-well plate at a density of 6×10^3 cells/well.

After 1 day, 3 days and 5 days of culture, the live/dead assay (Calcein-AM/PI stain kit) was used to evaluate cell survival and adhesion. Afterwards, an inverted fluorescence microscope was applied to capture the images.

To further evaluate the cell proliferation on different types of radially graded scaffolds, MC3T3-E1 cells at a density of 2×10^4 cells/well were seeded on four types of scaffolds with 75 % porosity in the 6-well plate. After 1, 3, and 5 days of incubation, the cell viability was evaluated by MTT assay.

2.7 Statistical analysis

All quantitative data obtained in this study was presented as mean value ± standard deviation. Statistical analysis for compressive strength and cell proliferation between experimental groups was performed using one-way ANOVA. $P<0.05$(*) was considered as significant difference.

3. Results and Discussion

3.1 Slurry properties

High solid loading and low viscosity are essential for ceramic slurry in VPP-based ceramic 3D printing. High solid loading could effectively avoid cracks in the debinding process, while low viscosity benefits the recoating process. Figure 3(a) shows the viscosity of current BCP slurry with 70 wt.% solid loading. Generally, the BCP slurry displayed an obvious shear thinning behavior, which benefited the slurry

storing and printing. It is well known that nano sized HAp particles can significantly increase the bioactivity and biocompatibility [34]. However, the addition of nano sized ceramic particles would increase the viscosity greatly due to their high specific surface area and surface energy [35, 36], which brings difficulties in the preparation of ceramic slurry containing nano-sized powders with high solid loading. In this study, the viscosity of 70 wt.% BCP slurry was about 600 mPa·s at 60 s^{-1} and was far below the critical value of the self-leveling (3000 mPa·s) [37]. This was mainly attributed to the optimal dispersant used, which was reported and discussed in our previous study [32].

To evaluate the curing ability of current BCP slurry and determine the optimal printing parameters for the subsequent printing, the relationship between cure depth and input energy dose was examined, as shown in figure 3(b). It could be described by the Beer-Lambert equation[38]:

$$C_d = D_p * \ln\left(\frac{E}{E_c}\right) \quad (12)$$

where C_d, D_p, E and E_c represent the cure depth, cure sensitivity of the slurry, input energy dose and critical exposure energy dose, respectively.

After data fitting in Origin software, it can be described as follows:

$$C_d = 188.5 * \ln\left(\frac{E}{6}\right) \quad (13)$$

The cure sensitivity value of the BCP slurry is 188.5, suggesting a high curing ability. To guarantee the strong interlayer bond in green parts, the cure depth should be at least twice of the printing layer thickness. Therefore, 35 μm was set as the printing layer thickness while ~10 mJ/cm^2 of energy dose with about 100 μm cure depth was employed in this study for the printing of radially graded scaffold.

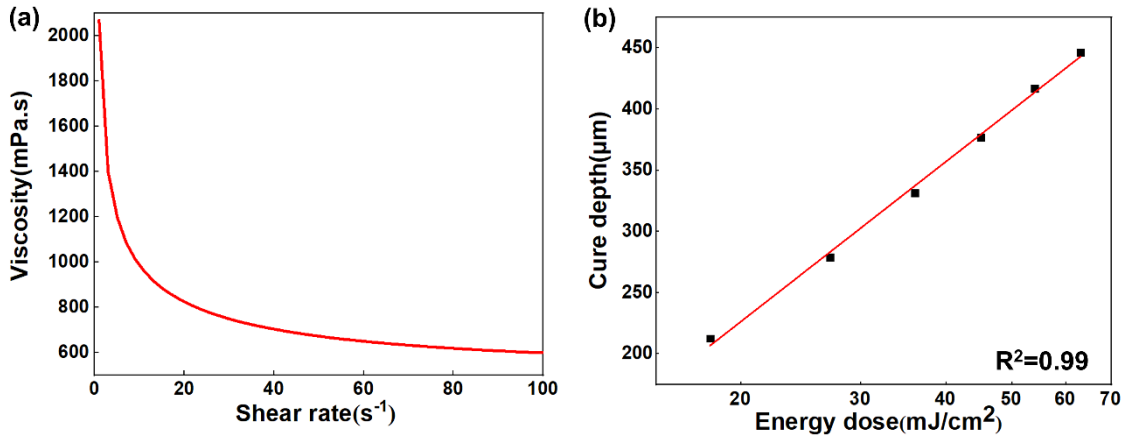

Figure 3. Properties of BCP slurry with 70 wt.% solid loading. (a) Viscosity. (b) Cure depth as a function of energy dose by the UV laser.

3.2 Post-processing of BCP green bodies

After printing, post-processing, including debinding and sintering, is necessary to obtain highly dense pure ceramic parts. Figure 4(a) shows the thermal decomposition behavior of the green body when heating from 50 ℃ to 700 ℃. Generally, the main weight loss happened between 300 and 600 ℃. There were three strong peaks observed at 330℃, 420 ℃ and 501℃, indicating the rapid decomposition of the polymer within the green body. Based on the TGA/DTG curve,

the debinding strategy was set as shown in figure 4(b). Principally, in the fast decomposition range (330℃-420℃ and 420℃-501℃), a low heating rate of 0.15℃/min should be applied to avoid cracks. A holding time at two peak points (330℃ and 420℃) was set to ensure complete removal of the polymer phases. After debinding, the BCP samples were heated to 1200 ℃ at 2 ℃/min and held for 2h to prepare the final BCP scaffolds.

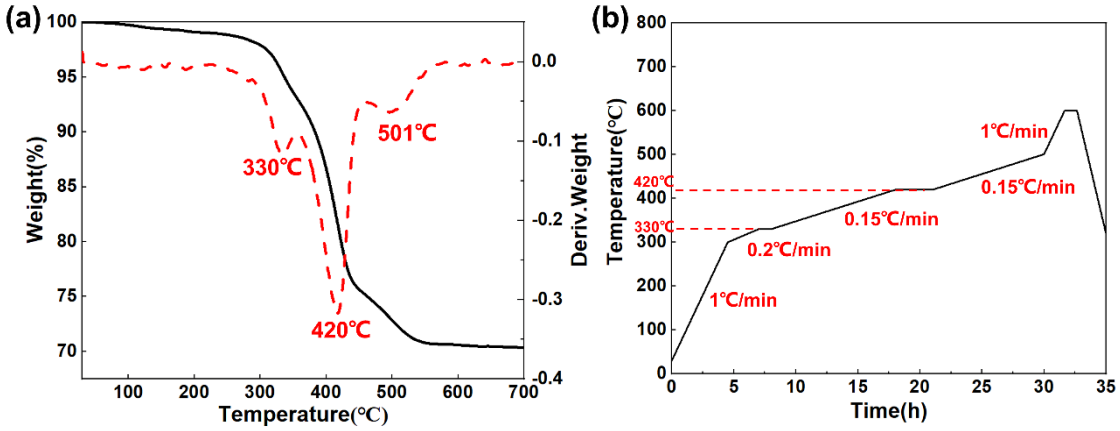

Figure 4. (a) Thermal decomposition of DLP-formed green body. (b) Debinding profile.

3.3 Morphological analysis of radially graded scaffolds

Four types of radially graded scaffolds (G-G, G-P, P-G, and P-P) with two porosity levels (65% and 75%) were designed and fabricated via DLP 3D printing. Top and side views of these scaffolds are shown in figure 5 (a-b) and figure 6 (a-b), respectively. Generally, the overall morphologies of sintered scaffolds were consistent with the 3D models with no obvious defects. Table 1 and 2 list the

geometrical parameters of CAD models and sintered porous BCP scaffolds. Compared to the initial CAD models, the pore size of the sintered scaffolds was smaller due to light scattering during photopolymerization and shrinkage in the sintering process [39, 40]. Porosity and pore size play a vital role in bone ingrowth and bone formation. A scaffold with higher porosity shows enhanced osteogenic outcomes [41]. However, as porosity increases, the mechanical properties of the scaffolds will decrease. The compromise between porosity and mechanical property should be carefully considered. Commonly, it was suggested that porosity of >60% was recommended for the design of a porous scaffold [42, 43]. Therefore, two porosity levels of 65% and 75% were designed for the radially graded scaffolds in the current study. For pore size design, macropores bigger than 300 μm are generally taken into consideration since they are beneficial for the formation of capillaries and osteointegration [41, 43]. After sintering, the porosities of G-G and G-P radially graded scaffolds were bigger than 60 vol.% in both two porosity groups while the real porosities of P-G and P-P scaffolds in 65% design group were slightly lower than the critical porosity value. Nevertheless, the pore sizes of all sintered scaffolds met the requirement of being larger than 300 μm, indicating that the current scaffolds could be suitable for BTE applications.

The G scaffolds showed better dimensional accuracy than the P scaffolds in both 65 vol.% and 75 vol.% groups. For example, despite the same designed pore size of 950 μm in the 75 vol.% group (inner pore size of G-G and G-P), the pore size of the P scaffold was about 845 μm. In comparison, the G scaffold was about 906 μm, demonstrating that the scattering in the P scaffold was higher than G. This could be mainly attributed to the inherent geometrical features of the structure. Pores of the G structure are formed by the curved surface whose center keeps changing in the plane. Therefore, the projection surface varies from layer to layer, which does not cause significant over-curing. While in the P structure, the pores are formed by undergoing same multiple exposures. The scattering accumulation between layers results in over-curing and poor accuracy. This phenomenon was also found in Shen's study [44]. Besides, the porosity of the sintered scaffolds was shown as G-G > G-P > P-G > P-P, indicating that the G structure was easier to maintain a higher similarity to CAD models than the P structure. Except for over-curing, some small pores in the transition area were blocked in P-P and P-G scaffolds (figure 5(d), red arrow). It should be noted that those small pores were generated automatically according to the mathematic equation and beyond the printing limitation of the DLP process. Fortunately, the outer and inner prominent pores maintained good structural integrity, as shown in figure 6(c-d), demonstrating that the methods and procedures established

in this study could fabricate BCP scaffolds with high design freedom and fabrication accuracy.

Table 1. Geometrical parameters of CAD models and sintered radially graded scaffolds with 75 vol.% porosity.

Scaffold	**Outer pore size (μm)**		**Inner pore size (μm)**		**Thickness* (μm)**		**Porosity (%)**	
	Design	Sintered	Design	Sintered	Design	Sintered	Design	Sintered
G-G	450	403.7±33.1	950	906.4±23.6	320	305.8±12.1	76	74.9±0.5
G-P	450	387.9±25.9	950	845.2±25.2	250	254.5±15.2	76	73.6±0.2
P-G	500	407.0±46.9	950	894.4±23.0	280	283.1±5.5	74	68.4±0.7
P-P	500	396.3±40.7	950	864.9±38.7	280	276.8±11.2	74	67.9±0.9

*The wall thickness of the TPMS surface.

Table 2. Geometrical parameters of CAD models and sintered radially graded scaffolds with 65 vol.% porosity.

Scaffold	**Outer pore size (μm)**		**Inner pore size (μm)**		**Thickness* (μm)**		**Porosity (%)**	
	Design	Sintered	Design	Sintered	Design	Sintered	Design	Sintered
G-G	400	344.0±23.9	800	738.6±39.6	500	480.7±9.5	65	64.5±0.1
G-P	450	374.1±16.1	850	727.7±11.3	375	368.8±9.7	65	63.0±0.6
P-G	500	364.9±28.8	850	791.1±21.0	375	358.7±25.1	67	59.5±0.2
P-P	500	397.8±21.4	850	712.7±6.4	300	291.6±11.1	67	57.5±0.6

* The wall thickness of the TPMS surface.

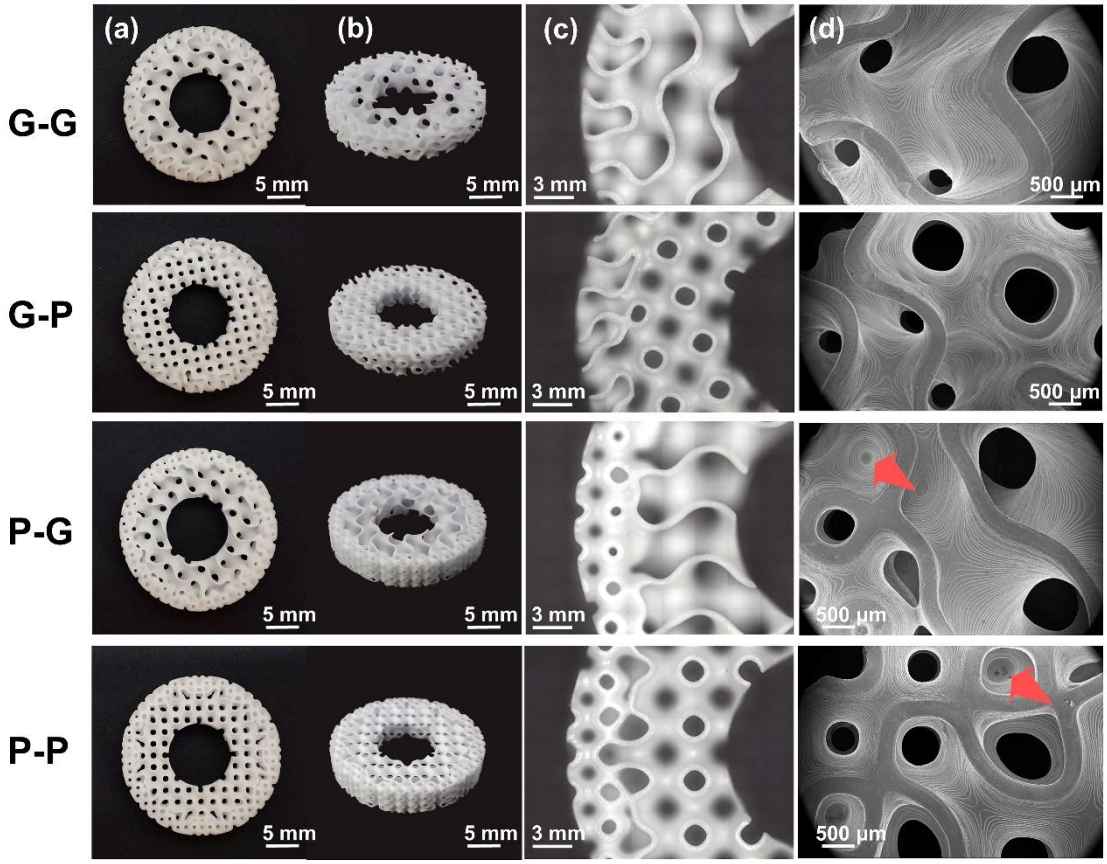

Figure 5. Morphologies of four types of radially graded scaffolds with 75 vol.% porosity. (a) Top view. (b) Side view. (c) Magnified view. (d) SEM images of the transitional area (Red arrow: blocked pores in the transition area).

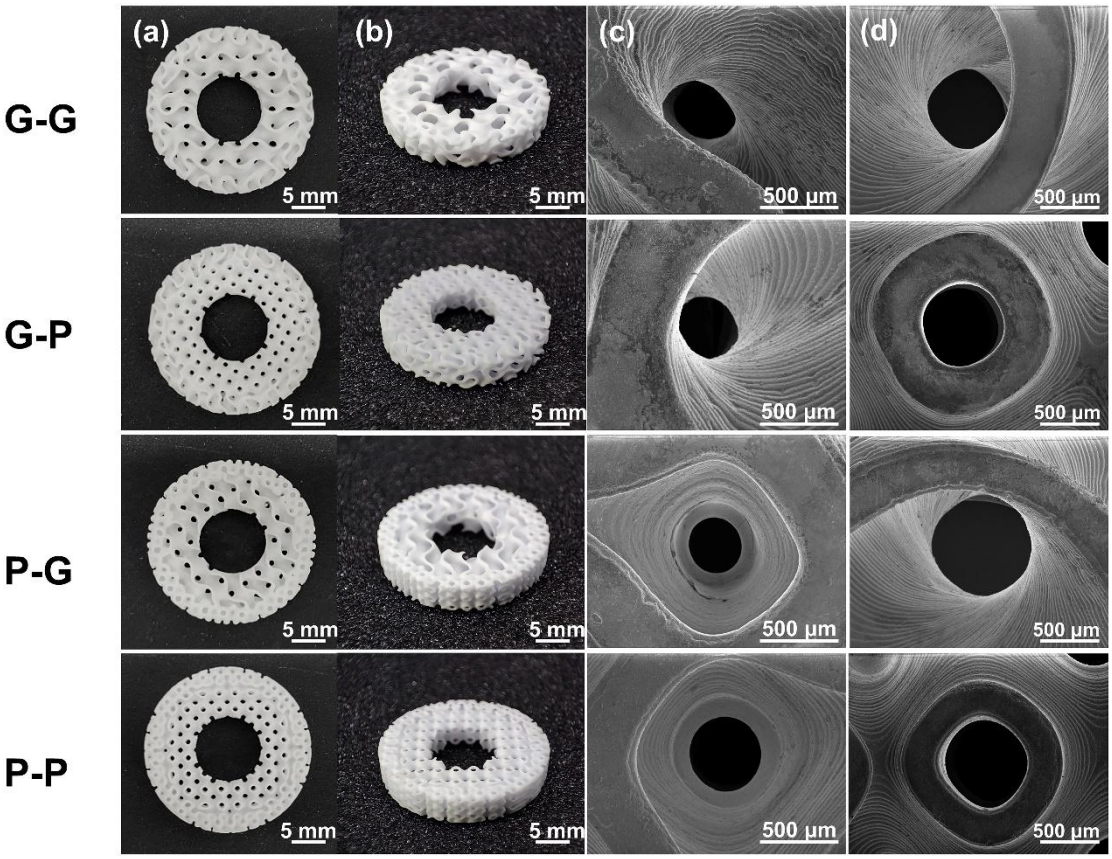

Figure 6. Morphologies of four types of radially graded scaffolds with 65 vol.% porosity. (a) Top view. (b) Side view. (c) Outer pore. (d) Inner pore

3.4 Microstructure and phase composition analysis

The sintering temperature highly influences the crystalline phase and physiochemical properties of the produced parts. Figure 7 shows the XRD pattern of the sintered BCP scaffolds. The strong peaks of HAp and β-TCP were detected obviously and had a good agreement with previous studies [35, 45]. The results showed that the BCP scaffolds fabricated via current process consisted only of HAp and β-TCP phases without dispersant or resin matrices, indicating that pure BCP scaffolds

were obtained after debinding and sintering treatment. The EDS map scanning results could also confirm the homogeneous distribution of Ca, P, and O without other elements (figure 8(a)). Besides, there were no standard peaks of α-TCP, indicating that the phase transformation to α-TCP in the sintering process did not occur. After high temperature sintering, the mass fraction of HAp and β-TCP was 45.7±0.7% and 54.3 ± 0.7%, respectively, which indicated that a small amount of HAp had transformed to β-TCP while most HAp maintained thermal stability. The high phase stability observed in our study could be attributed to the high-quality of starting materials. High purity and optimal Ca-to-P weight ratio could inhibit the phase transformation of HAp [46]. Therefore, the DLP-formed BCP scaffolds in this study could offer high bioactivity for BTE applications.

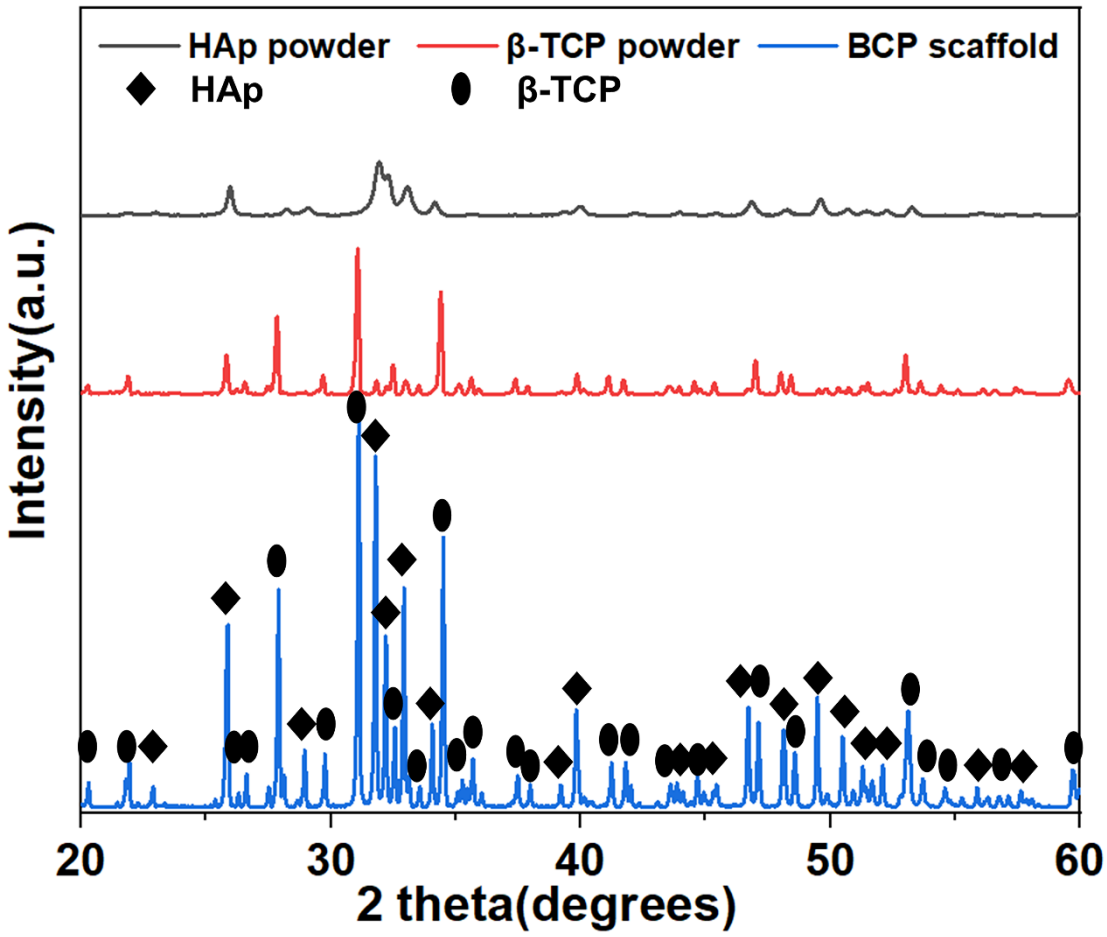

Figure 7. XRD pattern of sintered BCP scaffolds.

The microstructure is essential to determine the mechanical property of the BCP scaffolds and further significantly affects the structural integrity. Figure 8(b-i) exhibits the surface microstructure of the sintered BCP scaffolds. After sintering, the HAp and β-TCP ceramic particles were tightly interconnected with each other without any voids. Meanwhile, the microstructure of the scaffolds from a cross-sectional view is shown in figure 8(b-ii). The scaffolds displayed a layer structure in the Z direction without apparent cracks or defects, demonstrating that the current

DLP printing process and post-processing strategy had good capabilities of fabricating BCP ceramic scaffolds with good structural integrity.

The volume density could indicate the densification of the sintered bulk BCP ceramics, and further reflect the densification of the graded scaffolds. After sintering at 1200 ℃ for 2 h, the volume density and corresponding relative density of the bulk BCP ceramics reached 3.06 ±0.01 g/cm ^{3} and 97.18% ± 0.26%, respectively. This demonstrated that a high level of densification was achieved in the current study, which may provide satisfactory structural supports for cell behaviors.

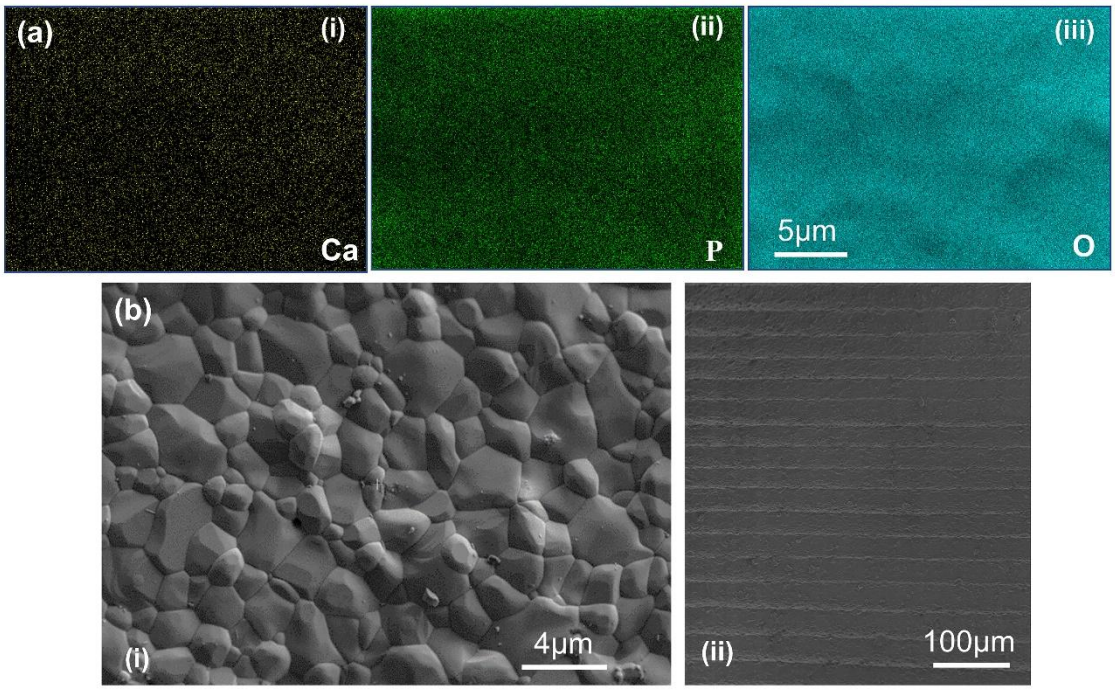

Figure 8. (a) Element distribution of sintered BCP scaffolds: (i) Ca map; (ii) P map; (iii) O map. (b) Microstructure of sintered BCP scaffolds: (i) surface microstructure; (ii) layer structure in a cross-sectional view.

3.5 Mechanical properties

A desirable BTE scaffold should possess sufficient compressive properties to maintain structural integrity and restore the native tissue functions after implantation. Figure 9 shows the compression stress-strain curves and compressive properties of four types of radially graded scaffolds with two porosity groups. Generally, the compressive stress gradually increased with the strain until reaching the ultimate compression strength. Some scaffolds exhibited a decrease in stress but followed by an increase again, mainly due to the deformities or small defects present in the scaffolds. As can be seen, for the same structure, the porosity had a significant effect on the compressive properties of the scaffolds. As the porosity rose, the mechanical properties dropped dramatically [47]. It was seen that both the compressive strength and modulus of 65 vol.% scaffolds were higher as compared to 75 vol.% groups. Furthermore, G-G and G-P scaffolds exhibited more robust compressive properties than P-G and P-P scaffolds. Because the radial design was that the inner region had a high porosity and the outer region had a low porosity, and the outer region bore the main loads when performed compression test. Therefore, the G structure could provide higher strength and modulus than the P structure when it is at the same porosity level. Vijayavenkataraman *et al*. investigated the effects of unit cell geometry and relative density on the mechanical properties of the scaffolds by

conducting finite element analysis. The results suggested that the G scaffolds had higher Young's modulus than P scaffolds with the same porosity [30]. Similarly, Shen *et al.* concluded that the structural characteristics could greatly influence the compressive strength of the porous structures derived from TPMS structure. For zirconia TPMS material fabricated via DLP process, the G structure showed a higher compressive strength than the P structure [44]. It is mainly because of the structure morphology difference. The G structure possesses a continuous curvature change on its surface, enabling a more uniform distribution of the stress. In contrast, the P structure has a large curvature change and obvious hollow areas in the middle, which easily cause stress concentration and are more likely to generate cracks and thus be wrecked [48, 49]. Besides, G structure displayed less sensitivity to structural defects and showed a stable mechanical performance, which was beneficial for engineering applications [44].

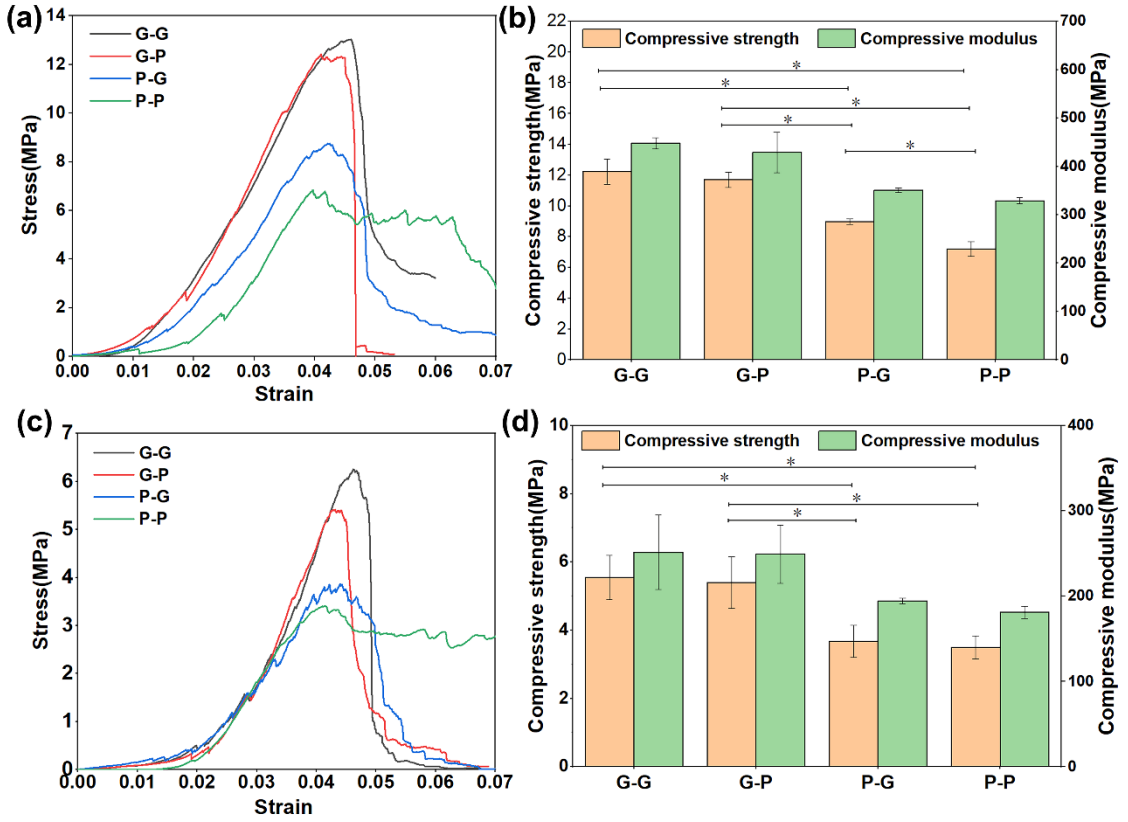

Figure 9. Compression stress-strain curves and compressive properties of radially graded scaffolds. (a) and (b) Scaffolds with 65 vol.% porosity. (c) and (d) Scaffolds with 75 vol.% porosity (* represents $P<0.05$).

To obtain a high-performance biomimicking radially graded scaffold, G-G structure was subsequently in-depth investigated since it possessed better dimensional accuracy and compressive property. Graded G-G scaffolds with various porosities (50%, 55%, 65%, and 75%) were designed and fabricated via DLP 3D printing (figure 10 (a)). The measured porosities of these scaffolds were 54.9%±0.6, 56.9%±0.5, 64.5±0.1, 74.9±0.5, respectively. Figure 10 (b) shows the relations between the designed porosity and measured porosity. Generally, the measured

porosity was roughly consistent with the designed porosity, which demonstrated that the high accuracy of current process to fabricate graded G-G scaffolds. Commonly, the effect of porosity exhibits an indirect proportionality on compressive strength, and sometimes logarithmic [50]. In this study, the compressive strength with different porosities and the best regression line drawn from the experimental data were shown in figure 10 (c). The regression equation can be described as:

$$y = -52.2 * \ln(x) + 230.4 \quad (14)$$

where x and y represent the porosity of the graded G-G scaffold and compressive strength under this porosity. The compressive strength of G-G scaffolds with designed porosities of 50 vol.%, 55 vol.%, 65 vol.% and 75 vol.% reached 23.55±2.39 MPa, 19.75±0.67 MPa, 12.23±0.82 MPa, and 5.55±0.65 MPa, respectively. The logarithmic trend was observed, and it could be used for predicting the compressive performance of BCP graded G-G scaffolds. Ryan *et al.* fabricated β-TCP scaffolds via VPP-based ceramic 3D printing and the effect of porosity on compressive strength also showed a logarithmic trend and had a good agreement with current study [51].

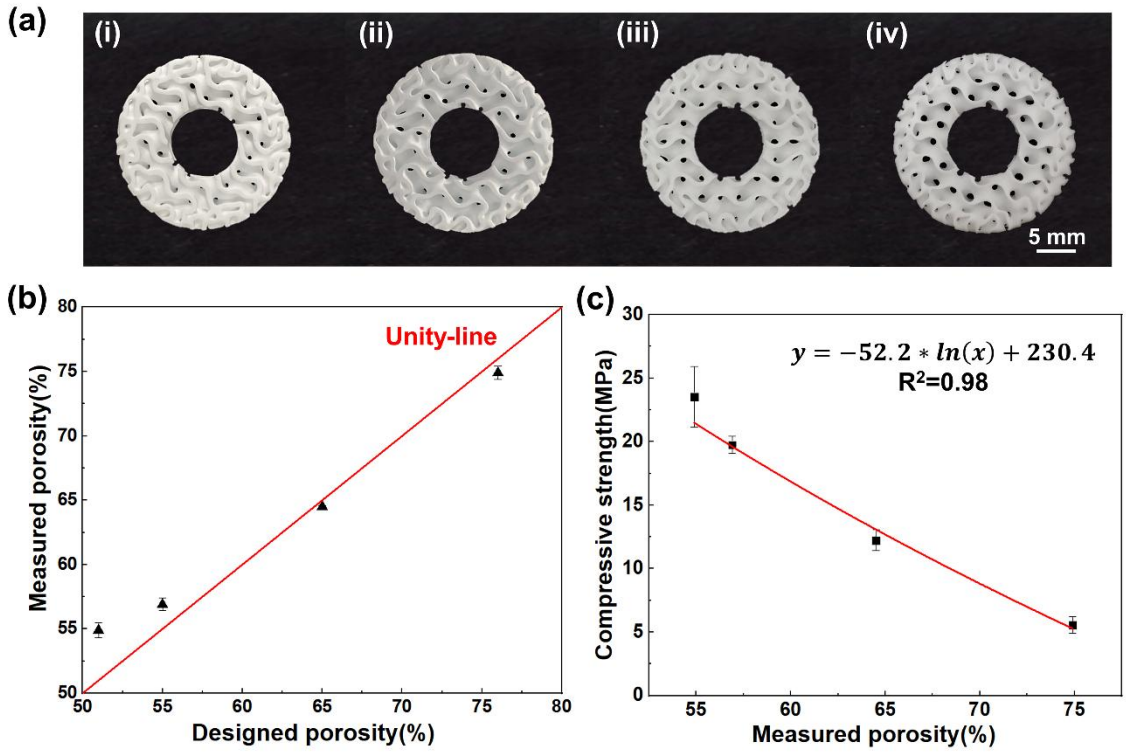

Figure 10. Graded G-G scaffolds with different porosities. (a) General view of the sintered scaffolds. (b) Relationship between designed and measured porosity (Unity-line is a modeled 1-to-1 correlation between designed porosity and measured porosity). (c) Compressive strength as a function of measured porosity.

Figure 11 displays the compressive strength of the porous calcium phosphate-based ceramic scaffolds with distinct porosities fabricated by VPP-based 3D printing that have been published in previous studies [35, 36, 52-58]. It could be seen that the BCP scaffold in this study exhibited better compressive properties than the calcium phosphate-based ceramic scaffolds (HAp, β-TCP, or CaP scaffolds) reported in the published studies. The first reason might be that high densification of the ceramic

grains was achieved after high-temperature sintering. Another reason could be attributed to the nano-sized ceramic powders used in BCP slurry since the refined ceramic grain size could increase the mechanical properties of the ceramic parts [59]. Lee *et al*. constructed BCP scaffolds with elongated G structures via DLP 3D printing. When the elongation was 60%, the compressive strength of scaffolds with 70 vol% porosity reached 11.51 ± 1.75 MPa (green triangle label)[35]. It demonstrated that the compressive properties could be improved through structural optimization. Therefore, if the elongated models were used in our study, the compressive strength may increase further. Overall, the mechanical properties of the BCP scaffolds in current study were comparable to human cancellous bone, which could potentially be used for BTE applications.

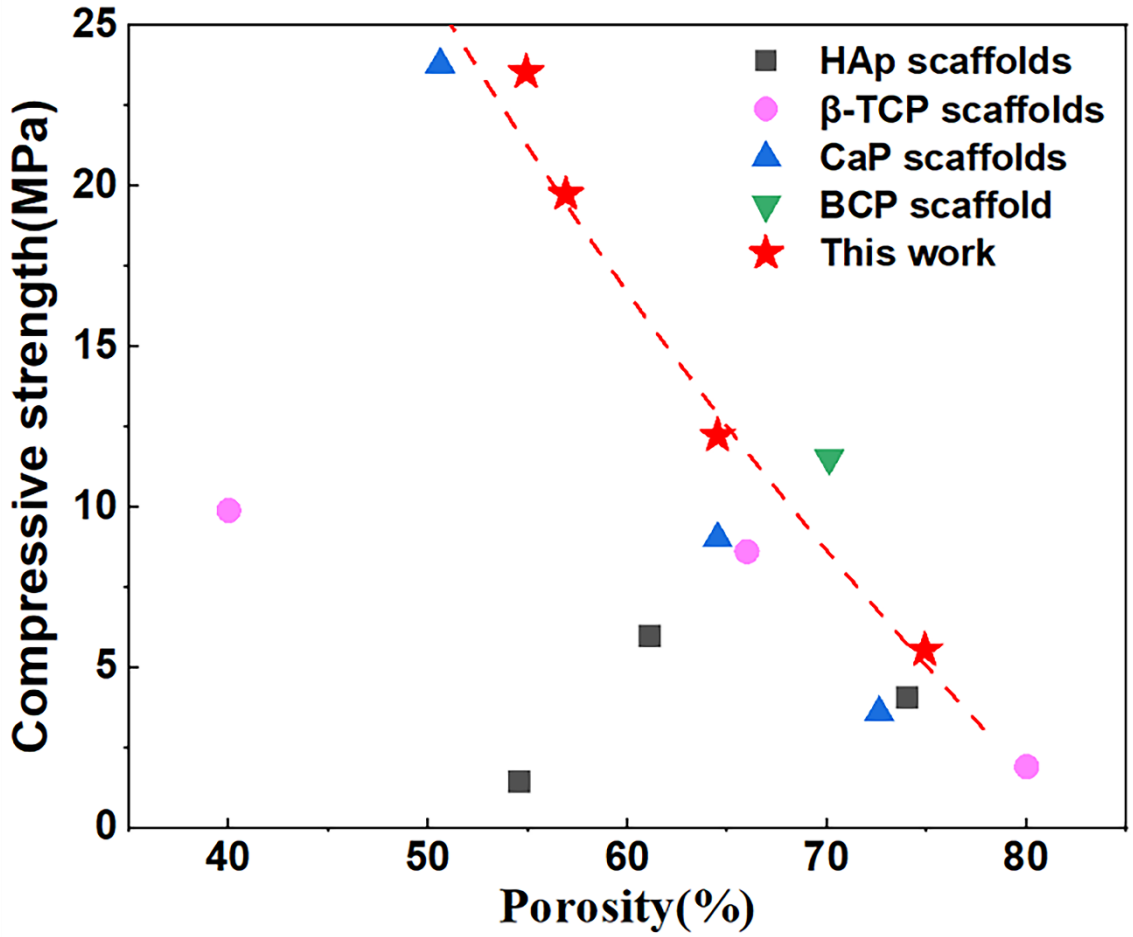

Figure 11. Comparison of compressive strength with different porosities of calcium phosphate-based ceramic scaffolds made by VPP based 3D printing (red curve: regression line derived from experimental results)

3.6 *In vitro* biological performance

In this study, MC3T3-E1 cells were used to study the *in vitro* biological properties. Figure 12(a) shows the *in vitro* cell proliferation behavior of MC3T3-E1 cells after being cultured for 1, 3, and 5 days on BCP disks. Generally, the BCP samples exhibited a similar proliferation rate to the control group, confirming that

the BCP bioceramic had excellent biocompatibility and could provide a favorable environment for cell behaviors. According to the live/dead staining (figure 12 (b)), the MC3T3-E1 cells could readily adhere to the BCP ceramic surface and maintain the normal cell morphologies after 1 day of incubation. The cell numbers gradually increased from day 1 to day 5 and showed more cell-cell interactions. MC3T3-E1 cells spread well with stretched morphologies and nearly formed a dense cell network after 5 days of culturing, demonstrating that the BCP bioceramics in current study were beneficial for cell adhesion, growth, and proliferation.

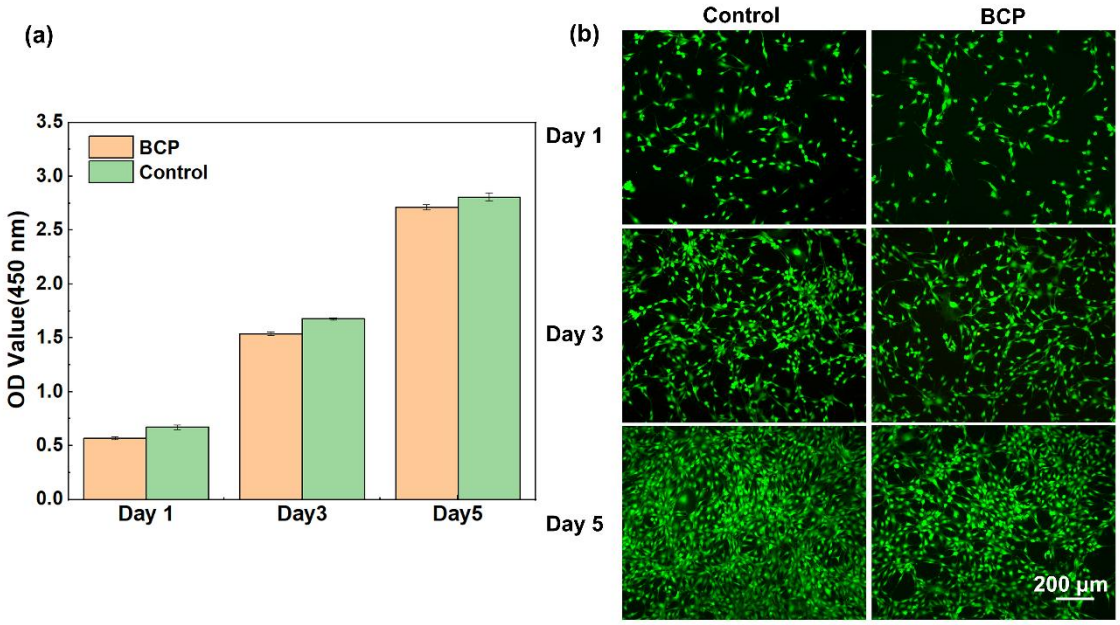

Figure 12. *In vitro* biological performance of sintered BCP bioceramics. (a) Proliferation of MC3T3-E1 cells after 1 day, 3 days and 5 days of incubation, respectively. (b) Viability of MC3T3-E1 cells after being cultured for 1 day, 3 days and 5 days, respectively.

To further compare the cell proliferation and viability on four types of scaffolds, MC3T3-E1 cells were seeded onto the scaffolds directly. Figure 13 shows the cell proliferation and proliferation rate with day 1 as normalization on different types of scaffolds. Generally, the OD value of scaffold group showed similar trend as compared to the control group in day 1. From day 3, the scaffold groups displayed more active cell behaviors and showed significant differences of cell proliferation as compared to control group on day 5, which was attributed to the complex 3D structures could provide more space for cell attachment, growth, and proliferation [60]. To minimize the effect of non-uniform cell distributions resulted from the seeding process, as shown in figure 13(b), the proliferation rate was normalized. G-G scaffolds exhibited the higher proliferation rate as compared to other scaffold groups, mainly owing to the inherent geometrical features. Yang *et al.* demonstrated that G structure could guide the cell fate through directional curvatures and thus enhance new bone formation [61].

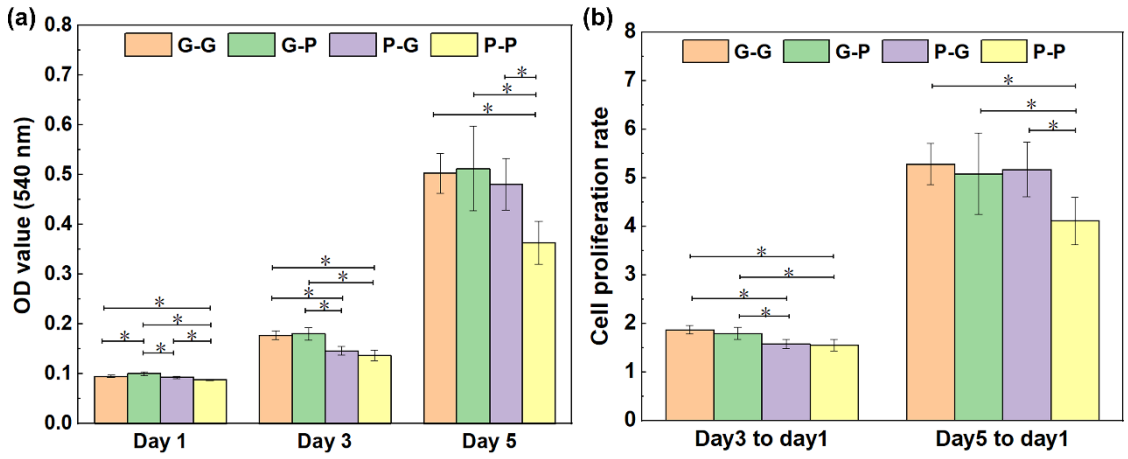

Figure 13. Cell proliferation on four types of scaffolds after 1 day, 3 days and 5 days of incubation. (a) MTT assay. (b) Cell proliferation rate (day 1 as normalization) (* represents $P<0.05$).

3.7 *In vitro* bioactivity evaluation

To study the potential bioactivity of the BCP scaffolds, BCP samples were immersed in the SBF solution to examine the apatite formation ability on the bioceramic surface [62, 63]. The surface morphology of the BCP bioceramics after being soaked in SBF solution for 3 days is shown in figure 14 (a). It was found that a layer of bone-like apatite entirely covered the surface of the BCP ceramic. In the magnified view, tiny apatite nanocrystals with porous structures were observed. A large amount of Ca, P, O, C, and a small amount of Mg were detected (figure 14(b)), demonstrating that carbonated calcium phosphate crystals were formed. The ability of biomaterials to form carbonate-containing apatite could evaluate the ability to bond with native

bone [64]. Therefore, the sintered BCP scaffolds in this study might have excellent bioactivity and perform a good interface behavior with native tissues *in vivo*.

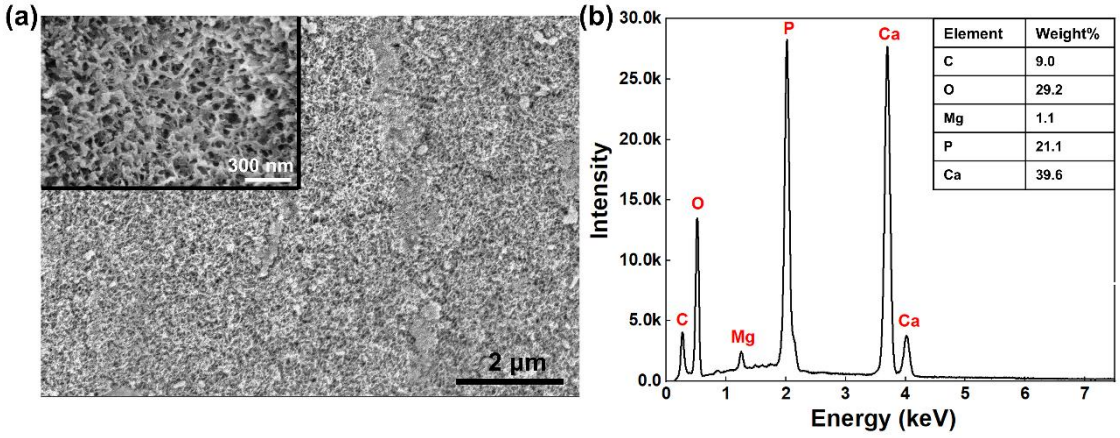

Figure 14. Bone-like apatite formation on the surface of BCP samples after immersion in SBF for 3 days. (a) SEM images. (b) EDS analysis.

4. Conclusions

In the current study, biomimicking radially graded BCP scaffolds for BTE were designed and successfully made through CAD and DLP 3D printing. The main conclusions include the following:

1) Four types of biomimicking radially graded scaffold designs based on TPMS-G and -P units were provided using a computer-assisted method. The porosity and pore size could be simultaneously controlled in a specific range via adjusting unit cell size and wall thickness.

2) The current BCP slurry formulation with 70 wt.% solid loading had a low viscosity (600 mPa·s at 60 s^{-1} shear rate) and high curing accuracy, which proved to be suitable for producing graded BCP scaffolds via 3D printing.

3) The G-G scaffolds had better dimensional accuracy, compressive property, and cell proliferation rate than the G-P, P-G, and P-P scaffolds. The relationship between compressive strength and porosity of graded G-G scaffold revealed a logarithmic trend and the G-G scaffold with 65 vol.% and 75 vol.% porosity could reach 12.23±0.82 MPa, 5.55±0.65 MPa, respectively.

4) This work has demonstrated an effective way to achieve biomimicking graded scaffold design based on TPMS units and accurate fabrication of the designed scaffolds via DLP 3D printing. The methods and procedures established in the current study help to advance the design of biomimicking BTE scaffolds and fabrication of complex bioceramic scaffolds.

Author contributions

Yue Wang: Methodology, Investigation, Formal analysis, Writing-original draft. Shangsi Chen: Methodology, Investigation. Haowen Liang: Validation. Jiaming Bai: Writing-review & editing, Supervision. Min Wang: Writing-review & editing, Supervision.

Conflicts of interest

There are no conflicts of interest to declare.

Acknowledgments

Y. Wang thanks Southern University of Science and Technology (SUSTech) for providing her with a PhD scholarship in the HKU-SUSTech Joint Education Programme for PhD. This work is supported by National Key R&D Program of China (2022YFE0197100), Shenzhen Science and Technology Innovation Commission [GJHZ20200731095606021; 20200925155544005; KQTD20190929172505711] and Hong Kong's Research Grants Council (RGC) through research grants (17200519, 17202921, 17201622 and N_HKU749/22). The authors acknowledge the support from SUSTech Core Research Facilities.

References

1. Y. Khan, M. J. Yaszemski, A. G. Mikos and C. T. Laurencin, *Jbjs*, 2008, **90**, 36-42.

2. J. L. Brown and C. T. Laurencin, in *Biomaterials Science*, Elsevier, 2020, pp. 1373-1388.

3. A. R. Amini, C. T. Laurencin and S. P. Nukavarapu, *Critical Reviews™ in Biomedical Engineering*, 2012, **40**.

4. S. Bose, M. Roy and A. Bandyopadhyay, *Trends in biotechnology*, 2012, **30**, 546-554.

5. L. Roseti, V. Parisi, M. Petretta, C. Cavallo, G. Desando, I. Bartolotti and B. Grigolo, *Materials Science and Engineering: C*, 2017, **78**, 1246-1262.

6. M. Zhang, R. Lin, X. Wang, J. Xue, C. Deng, C. Feng, H. Zhuang, J. Ma, C. Qin and L. Wan, *Science advances*, 2020, **6**, eaaz6725.

7. Y.-Z. Xiong, R.-N. Gao, H. Zhang, L.-L. Dong, J.-T. Li and X. Li, *Journal*

of the mechanical behavior of biomedical materials, 2020, **104**, 103673.

8. S. Ma, K. Song, J. Lan and L. Ma, *Journal of the mechanical behavior of biomedical materials*, 2020, **107**, 103727.

9. E. Salimi, *Ceramics International*, 2020, **46**, 19664-19668.

10. S. M. Bittner, B. T. Smith, L. Diaz-Gomez, C. D. Hudgins, A. J. Melchiorri, D. W. Scott, J. P. Fisher and A. G. Mikos, *Acta biomaterialia*, 2019, **90**, 37-48.

11. F. Gao, Z. Xu, Q. Liang, B. Liu, H. Li, Y. Wu, Y. Zhang, Z. Lin, M. Wu and C. Ruan, *Advanced Functional Materials*, 2018, **28**, 1706644.

12. X.-Y. Zhang, X.-C. Yan, G. Fang and M. Liu, *Additive Manufacturing*, 2020, **32**, 101015.

13. Y. Li, H. Jahr, P. Pavanram, F. S. L. Bobbert, U. Puggi, X. Y. Zhang, B. Pouran, M. A. Leeflang, H. Weinans, J. Zhou and A. A. Zadpoor, *Acta Biomaterialia*, 2019, **96**, 646-661.

14. K. S. Ødegaard, J. Torgersen and C. W. Elverum, *Metals*, 2020, **10**, 1677.

15. J. Wang, Y. Peng, M. Chen, X. Dai, L. Lou, C. Wang, Z. Bao, X. Yang, Z. Gou and J. Ye, *Bioactive Materials*, 2022.

16. R. LeGeros, S. Lin, R. Rohanizadeh, D. Mijares and J. LeGeros, *Journal of materials science: Materials in Medicine*, 2003, **14**, 201-209.

17. S. Chen, Y. Shi, X. Zhang and J. Ma, *Materials Science and Engineering: C*, 2020, **112**, 110893.

18. S. Chen, Y. Shi, X. Zhang and J. Ma, *Ceramics International*, 2019, **45**, 10991-10996.

19. J. M. Bouler, P. Pilet, O. Gauthier and E. Verron, *Acta Biomaterialia*, 2017, **53**, 1-12.

20. H. Chen, W. Dou, Q. Zhu, D. Jiang, J. Xia, X. Wang, W. Tang and S. Wang, *Materials Research Express*, 2019, **6**, 125412.

21. Z. Liu, H. Liang, T. Shi, D. Xie, R. Chen, X. Han, L. Shen, C. Wang and Z. Tian, *Ceramics International*, 2019, **45**, 11079-11086.

22. B. Guo, X. Ji, X. Chen, G. Li, Y. Lu and J. Bai, *Virtual and Physical Prototyping*, 2020, **15**, 520-531.

23. S. Limmahakhun, A. Oloyede, K. Sitthiseripratip, Y. Xiao and C. Yan, *Materials & Design*, 2017, **114**, 633-641.

24. F. Liu, Z. Mao, P. Zhang, D. Z. Zhang, J. Jiang and Z. Ma, *Materials & Design*, 2018, **160**, 849-860.

25. G. Wang, L. Shen, J. Zhao, H. Liang, D. Xie, Z. Tian and C. Wang, *ACS*

Biomaterials Science & Engineering, 2018, **4**, 719-727.

26. J. Shi, L. Zhu, L. Li, Z. Li, J. Yang and X. Wang, *Scientific Reports*, 2018, **8**, 7395.

27. Q. Zhang, L. Ma, X. Ji, Y. He, Y. Cui, X. Liu, C. Xuan, Z. Wang, W. Yang and M. Chai, *Advanced Functional Materials*, 2022, 2204182.

28. S. Vijayavenkataraman, L. Y. Kuan and W. F. Lu, *Materials & Design*, 2020, **191**, 108602.

29. S. Yu, J. Sun and J. Bai, *Materials & Design*, 2019, **182**, 108021.

30. S. Vijayavenkataraman, L. Zhang, S. Zhang, J. Y. Hsi Fuh and W. F. Lu, *ACS Applied Bio Materials*, 2018, **1**, 259-269.

31. C. Gupta, N. Nayak, S. G. Kalthur and A. S. D'Souza, *Saudi Journal of Sports Medicine*, 2015, **15**, 244.

32. Y. Wang, S. Chen, H. Liang, Y. Liu, J. Bai and M. Wang, *Ceramics International*, 2022.

33. H. Liang, Y. Wang, S. Chen, Y. Liu, Z. Liu and J. Bai, *International Journal of Bioprinting*, 2022, **8**.

34. M. Sadat-Shojai, M.-T. Khorasani, E. Dinpanah-Khoshdargi and A. Jamshidi, *Acta biomaterialia*, 2013, **9**, 7591-7621.

35. J.-W. Lee, Y.-H. Lee, H. Lee, Y.-H. Koh and H.-E. Kim, *Ceramics International*, 2021, **47**, 3252-3258.

36. Y. Wei, D. Zhao, Q. Cao, J. Wang, Y. Wu, B. Yuan, X. Li, X. Chen, Y. Zhou and X. Yang, *ACS Biomaterials Science & Engineering*, 2020, **6**, 1787-1797.

37. X. Chen, J. Sun, B. Guo, Y. Wang, S. Yu, W. Wang and J. Bai, *Ceramics International*, 2022, **48**, 1285-1292.

38. M. L. Griffith and J. W. Halloran, *Journal of the American Ceramic Society*, 1996, **79**, 2601-2608.

39. S. A. Rasaki, D. Xiong, S. Xiong, F. Su, M. Idrees and Z. Chen, *Journal of Advanced Ceramics*, 2021, **10**, 442-471.

40. G. Mitteramskogler, R. Gmeiner, R. Felzmann, S. Gruber, C. Hofstetter, J. Stampfl, J. Ebert, W. Wachter and J. Laubersheimer, *Additive Manufacturing*, 2014, **1**, 110-118.

41. V. Karageorgiou and D. Kaplan, *Biomaterials*, 2005, **26**, 5474-5491.

42. B. Zhang, X. Pei, C. Zhou, Y. Fan, Q. Jiang, A. Ronca, U. D'Amora, Y. Chen, H. Li and Y. Sun, *Materials & Design*, 2018, **152**, 30-39.

43. Y. Zhang, N. Sun, M. Zhu, Q. Qiu, P. Zhao, C. Zheng, Q. Bai, Q. Zeng and

T. Lu, *Biomaterials Advances*, 2022, **133**, 112651.

44. M. Shen, W. Qin, B. Xing, W. Zhao, S. Gao, Y. Sun, T. Jiao and Z. Zhao, *Journal of the European Ceramic Society*, 2021, **41**, 1481-1489.

45. J. Wang, Y. Tang, Q. Cao, Y. Wu, Y. Wang, B. Yuan, X. Li, Y. Zhou, X. Chen, X. Zhu, C. Tu and X. Zhang, *Regenerative Biomaterials*, 2022.

46. F. Baino, G. Magnaterra, E. Fiume, A. Schiavi, L. P. Tofan, M. Schwentenwein and E. Verné, *Journal of the American Ceramic Society*, 2022, **105**, 1648-1657.

47. C. Torres-Sanchez, F. R. A. Al Mushref, M. Norrito, K. Yendall, Y. Liu and P. P. Conway, *Materials Science and Engineering: C*, 2017, **77**, 219-228.

48. P. Sengsri and S. Kaewunruen, *Materials Today: Proceedings*, 2022, **65**, 1656-1659.

49. J. Lu, P. Dong, Y. Zhao, Y. Zhao and Y. Zeng, *Ceramics International*, 2021, **47**, 12897-12905.

50. A. J. W. Johnson and B. A. Herschler, *Acta biomaterialia*, 2011, **7**, 16-30.

51. E. Ryan and S. Yin, *Ceramics International*, 2022, **48**, 15516-15524.

52. Y. S. Cho, S. Yang, E. Choi, K. H. Kim and S.-J. Gwak, *Ceramics International*, 2021, **47**, 35134-35143.

53. C. Feng, K. Zhang, R. He, G. Ding, M. Xia, X. Jin and C. Xie, *Journal of Advanced Ceramics*, 2020, **9**, 360-373.

54. X. Huang, H. Dai, Y. Hu, P. Zhuang, Z. Shi and Y. Ma, *Journal of the European Ceramic Society*, 2021, **41**, 3743-3754.

55. Y.-H. Lee, J.-B. Lee, W.-Y. Maeng, Y.-H. Koh and H.-E. Kim, *Journal of the European Ceramic Society*, 2019, **39**, 4358-4365.

56. S. Liu, L. Mo, G. Bi, S. Chen, D. Yan, J. Yang, Y.-G. Jia and L. Ren, *Ceramics International*, 2021, **47**, 21108-21116.

57. Y. Yao, W. Qin, B. Xing, N. Sha, T. Jiao and Z. Zhao, *Journal of Advanced Ceramics*, 2021, **10**, 39-48.

58. F. Zhang, J. Yang, Y. Zuo, K. Li, Z. Mao, X. Jin, S. Zhang, H. Gao and Y. Cui, *Materials & Design*, 2022, **216**, 110558.

59. P. Palmero, *Nanomaterials*, 2015, **5**, 656-696.

60. M. Shen, Y. Li, F. Lu, Y. Gou, C. Zhong, S. He, C. Zhao, G. Yang, L. Zhang and X. Yang, *Bioactive Materials*, 2023, **25**, 374-386.

61. Y. Yang, T. Xu, H.-P. Bei, L. Zhang, C.-Y. Tang, M. Zhang, C. Xu, L. Bian, K. W.-K. Yeung and J. Y. H. Fuh, *Proceedings of the National Academy of Sciences*,

2022, **119**, e2206684119.

62. A. A. Zadpoor, *Materials Science and Engineering: C*, 2014, **35**, 134-143.

63. T. Kokubo and H. Takadama, *Biomaterials*, 2006, **27**, 2907-2915.

64. S. Yu, K. P. Hariram, R. Kumar, P. Cheang and K. K. Aik, *Biomaterials*, 2005, **26**, 2343-2352.